Journal of Petroleum Science and Engineering 221 (2023) 111262

Contents lists available at ScienceDirect

Journal of Petroleum Science and Engineering

journal homepage: www.elsevier.com/locate/petrol

Application of multicomponent sorption for diffusive transport in numerical simulation of tight reservoirs

Sofiane H. Achour, Ryosuke Okuno *

Hildebrand Department of Petroleum and Geosystems Engineering, The University of Texas at Austin 200 E. Dean Keeton Street, Stop C0300, Austin, TX, 78712, USA

ARTICLE INFO

Keywords:
Diffusion
Sorption
Potential theory
Dusty gas model
Tight formation

ABSTRACT

One of the main challenges in modeling compositional transport in tight formations is to include the complex interaction of chemical species with rock surfaces. Such interactions result in compositional variations near the surfaces, which can significantly affect the compositional diffusive transport through tight pores.

This paper presents the application of the Multicomponent Potential Theory of Adsorption (MPTA) for the fluid compositions in the central and near-wall sorbed layers subject to a wall chemical potential. The two-layer approximation of MPTA is implemented in the diffusive transport simulation that computes the mass transfer driven by fugacity gradient based on the dusty gas model for the central and sorbed layers of pores. This simulator uses a partially implicit formulation to solve the multiphase multicomponent mass transfer equations including the sorbed layer.

The main novelty of this paper lies in the detailed analysis of the interplay between fluid components and rock surfaces, which became possible with the two-layer MPTA coupled with multicomponent diffusion. The diffusion simulation for a ternary case of methane, n-butane, and n-decane with the approximate MPTA shows that the sorption and capillary pressure can cause the compositional segregation between the central and sorbed layers. The segregation enhances the rates of methane injection and n-decane production in their counter-current diffusion. Methane (the lightest) is transported deep into the reservoir by diffusing through the central layer while n-decane (the heaviest) is diffused primarily through the sorbed layer. n-Butane (the intermediate) does not show preferential partitioning into either layer, resulting in relatively inefficient transport. In the absence of sorption and capillary pressure, the countercurrent diffusion occurs between methane (the lightest) and n-butane (the intermediate) while n-decane (the heaviest) remains nearly immobile. That is, whether the simulation considers the surface-fluid interactions can substantially affect the compositional transport (e.g., produced fluid composition) through tight porous media.

The multicomponent Langmuir model is often used for computing the sorbed excess in micropores. However, results show that the Langmuir model becomes physically inconsistent at high pressures because it predicts a monotonically increasing function of pressure. The new approach developed in this research is sufficiently flexible and reasonably accurate for modeling multicomponent sorption at high pressures.

1. Introduction

Advances in hydraulic fracturing enabled the development of previously inaccessible oil and gas in tight reservoirs. The primary recovery from such reservoirs has been inefficient (Gherabati et al., 2018). Therefore, gas injection, often with a cyclic injection-production scheme, has been pilot tested and implemented to increase the production. However, the existing theory and experience in gas injection for conventional reservoirs may not be entirely applicable to these tight reservoirs because fluids and their transport through small pores can substantiate different physical phenomena, such as sorption and capillary pressure.

Sorption alters the fluid density and composition distribution across pores and the transport coefficients. The most widely used model for those phenomena is the Multicomponent Langmuir (ML) model for the number of excess moles caused by the interaction with the pore wall and the surface diffusion coefficients for the transport of sorbed species. ML assumes a fixed number of sorption sites and a constant kinetic rate of

* Corresponding author.
E-mail addresses: sachour@utexas.edu (S.H. Achour), okuno@austin.utexas.edu (R. Okuno).

https://doi.org/10.1016/j.petrol.2022.111262
Received 30 July 2022; Received in revised form 11 September 2022; Accepted 16 November 2022
Available online 14 December 2022

adsorption and desorption. The mathematical expression derived for ML predicts the additional (or "excess") number of moles sorbed on the pore wall caused by sorption. ML shows a monotonically increasing number of excess moles with pressure and an asymptotic excess mole number (Butt et al., 2003).

The main advantage of ML is that its simple formulation can be directly implemented in a flash calculation (Sandoval et al., 2018) or a reservoir simulator (Cao, 2018; Computer Modelling Group, 2016). As will be shown in this paper, however, the asymptotically increasing function of pressure causes physically inconsistent sorption at high pressures. Also, molecular dynamics simulations of oil mixtures showed that these mixtures do not form a single layer of adsorbed molecules per sorption site unlike the single-layer assumption of ML; rather, the fluid density continuously changes from the pore wall to the pore center because of the interaction of fluid molecules with the pore walls (Baek and Akkutlu, 2019). Some modifications to the standard ML model have been used (Sandoval et al., 2018; Weniger et al., 2010) to better match dense gases and liquids that do not fit the standard ML. However, no evidence has been shown that these modifications work accurately for multicomponent mixtures at high pressures and temperatures. Moreover, there is no framework for efficient computation of adsorption of liquid-like heavy hydrocarbons in reservoir simulators. One of the objectives of this paper is to provide a suitable methodology for estimating sorption in multicomponent liquid mixtures in tight reservoirs.

More fundamental approaches to computing the effect of sorption consist of computing the full density and composition distribution across a pore based on an equation of state and a wall potential (Jin and Firoozabadi, 2016; Ma and Jamili, 2016; Sandoval et al., 2018). Implementations of this approach are based on the Multicomponent Potential Theory of Adsorption (MPTA) (Shapiro and Stenby, 1998), the Simplified Local Density (SLD) (Rangarajan et al., 1995), and the Engineering Density Functional Theory (EDFT) (Evans, 1979). However, this approach is generally computationally expensive and has not been used in reservoir simulators for reservoir-scale calculation. To our knowledge, the only example of such implementation is that of Cihan et al. (2019). However, their approach is computationally expensive and unlikely feasible for reservoir-scale simulation.

Fickian surface-diffusion models have been used to compute the flow of sorbed species in tight porous media (Shen et al., 2018a). Akkutlu and Fathi (2012) were the first to implement this model in a compositional reservoir simulator to compute mass transfer in shales and found that gas surface diffusion can become the dominant transport mechanism. Many authors including Wu et al. (2016), Shen et al. (2018b), Zhang et al. (2020) calibrated Fickian surface-diffusion model on experimental measurements of transport rates in shale cores and showed that this mechanism dominates total gas mass transfer in nanopores, especially in the presence of high organic pores content.

These surface diffusion models are based on Fick's law except that the driving force is the concentration gradient on the pore wall as given by the sorption model. It is straightforward to derive an analytical solution to it or implement it in a reservoir simulator because of the simplicity of Fick's law. However, this approach requires the calibration of many transport parameters that cannot be experimentally decoupled from other transport parameters, such as permeability, slip length, and diffusion coefficients. Many calibration parameters tend to cause a risk of over-fitting. In addition, all Fickian surface-diffusion models were developed and calibrated for surface transport of pure methane or other dry natural gases. There is no existing framework for modeling surface transport in the presence of liquid mixtures in a reservoir simulator. This paper presents a new approach to modeling surface transport that can be applied to any mixture including liquids by coupling the diffusive transport model calibrated with the measured transport coefficients for bulk fluid mixtures and the sorption model that computes the density of a sorbed layer.

This paper presents the first simulation model that can capture the enhanced segregated transport during gas injection in tight porous media by properly including sorption in the equilibrium and transport equations. The MPTA method is applied with a discretized pore consisting of two regions to compute the equilibrium at a constant total pore volume and number of moles. In each region, a flash calculation minimizes the Helmholtz free energy at a fixed volume and number of moles while including the effect of capillary pressure (Achour and Okuno, 2021). The simulator models thermodynamic fluid properties using the Peng-Robinson equation of state (PREOS) (Robinson and Peng, 1978). The flow simulator uses the Dusty Gas Model (Achour and Okuno, 2022) to compute the diffusion coefficients in the bulk and sorbed layers based on the corresponding thermodynamic state variables.

2. Method

This section presents the formulation for solving the equilibrium composition distribution across a discretized pore subject to a wall potential at a fixed temperature, the total number of moles, and volume based on the MPTA. Then, it introduces the algorithm used to solve this problem. Finally, it explains how the MPTA algorithm is implemented in our in-house, Tight Reservoir Simulator (TigReS), to solve the mole balance equations for both layers to compute the fluxes between grid blocks at each time step.

In this paper, the term "regions" refers to the discretized pore volumes used to calculate the equilibrium pore composition distribution, and the term "grid blocks" refers to discretized reservoir rock volumes used in transport simulations.

This simulator is based on individually validated models. The numerical diffusion simulation in nanopores was validated against experimental measurements in Achour and Okuno (2022). The sorption model parameters were calibrated by Sandoval et al. (2018) based on experiments with Marcellus shale cores conducted by Wang et al. (2015). The validation of the entire simulator based on huff-and-puff experiments with shale cores requires the coupling of diffusion with Darcy flow, which is outside the scope of this paper.

2.1. Formulation

The MPTA (Shapiro and Stenby, 1998) formulates the equilibrium in a pore as the solution to the equation

$$\ln f_{i,r} - \frac{\varepsilon_{i,r}}{RT} = \ln f_{i,N_r} \tag{1}$$

where i = 1,...,N_C and r = 1, ..., (N_r-1) for N_c components and N_r regions. R, T, $f_{i,r}$, and $\varepsilon_{i,r}$ are the universal gas constant, temperature, fugacity, and wall potential for component i in region r. The solution of Equation (1) is subject to two types of constraints. The first type constrains the entire pore, and includes the mole balance

$$n_i = \sum_{r=1}^{N_r} n_{i,r} \tag{2}$$

where i = 1,...,N_C and volume balance

$$V = \sum_{r=1}^{N_r} V_r \tag{3}$$

where n_i, V, $n_{i,r}$ and V_r are the total number of moles of component i, the total pore volume, the number of moles of component i in region r, and the volume V_r of region r. The second type constrains each region, and consists of the minimum number of moles,

$$n_{i,r} > 0 \tag{4}$$

where i = 1,...,N_C and r = 1,...,N_r, and minimum molar volume constraints,

$$\sum_{i=1}^{N_c} n_{i,r} b_i < V_r \tag{5}$$

where r = 1,…,Nr.

In the above, b_i is the co-volume parameter for the cubic equation of state assuming van der Waals mixing rules.

This problem has $N_c(N_r - 1)$ independent variables $\omega_{i,r}$ ($i = 1, \ldots, N_c$ and $r = 1, \ldots, N_r - 1$). The gradient vector can be derived by rewriting Equation (1) as

$$g_{i,r}^S = \ln f_{i,r} - \frac{\varepsilon_{i,r}}{RT} - \ln f_{i,N_r} \tag{6}$$

where i = 1,…,NC and r = 1,…,(Nr−1).

The Jacobian matrix is the derivative of (6) with respect to the independent variables $\omega_{i,r}$

$$J_{(i,j),(j,s)} = n_j \left(\delta_{r,s} \left(\frac{\partial \ln f_{i,r}}{\partial n_{j,r}} - \frac{\partial}{\partial n_{j,r}} \left(\frac{\varepsilon_{i,r}}{RT} \right) \right) + \frac{\partial \ln f_{i,N_r}}{\partial n_{j,N_r}} + \frac{\partial}{\partial n_{j,N_r}} \left(\frac{\varepsilon_{i,N_r}}{RT} \right) \right), \tag{7}$$

where $i = 1, \ldots, N_c$, $j = 1, \ldots, N_c$, $r = 1, \ldots, N_r$, $s = 1, \ldots, N_r$, and $\delta_{r,s}$ is the Kronecker delta function which is 1 if $r = s$ and 0 otherwise. Appendix A provides derivations for the analytical expressions for the derivatives of the logarithm of the fugacity.

The calculations presented in this paper use the Dubinin-Radushkevich-Astakhov (DRA) (Dubinin, 1985) wall potential

$$\varepsilon_{i,r} = \varepsilon_{i0} \left(\ln \left(\frac{z_0}{z} \right) \right)^{1/\beta} \tag{8}$$

where i = 1,…,NC.

In Equation (8), β and ε_{i0} are calibration parameters, and z_0 and z are the total pore volume per mass of solid rock and the volume of fluid between the pore wall and a certain point in the pore per mass of solid rock. Equation (8) can be rewritten as $\varepsilon_{i,r} = \varepsilon_{i0}(\ln(\zeta))^{1/\beta}$ as a function of a dimensionless volume $\zeta = z/z_0$, which varies from 0 (on the pore wall) to 1 (at the pore center). The DRA potential is not a function of the number of moles in the discretized pore region; therefore, its derivative is

$$\frac{\partial \varepsilon_{i,r}}{\partial n_{j,r}} = \frac{\partial \varepsilon_{i,N_r}}{\partial n_{j,N_r}} = 0. \tag{9}$$

2.2. Algorithm

The algorithm uses the Newton-Raphson method to solve Equation (1) using a nested loop of flash calculations based on Dawass et al. (2016). Unlike Dawass et al. (2016), however, we enforce constraints Equations (4) and (5) by using an underrelaxation method without removing a component from the region completely. Dawass et al.'s (2016) algorithm also assumes that each region contains a single phase only. The algorithm presented in this paper uses the isothermal-isochoric flash calculation including the capillary pressure to compute the phase equilibrium in each region (Achour and Okuno, 2020).

The initial guesses are set to $\omega_{i,r} = 1/N_r$ ($i = 1, \ldots, N_c$, and $r = 1, \ldots, N_r$) when initializing the simulation. During the flow simulation, however, the simulator uses $\omega_{i,r}$ from the previous timestep or the previous Newton update of the mole balance equations as the initial guess. A description of the sequential iteration scheme is presented below, and followed by some details on steps 3, 4, and 5.

Step 1. Run flash calculations for each region at a fixed number of moles $n_{i,r}$ and volume V_r where $i = 1, \ldots, N_c$ and $r = 1, \ldots, N_r$.

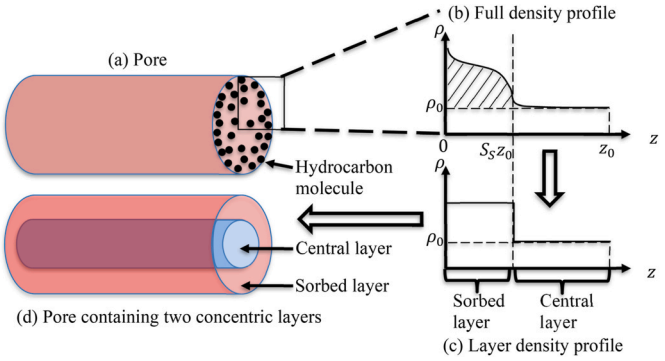

Fig. 1. Schematic of a pore split into the central and sorbed layers.

Step 2. Calculate the gradient g^S using Equation (6) and the Jacobian matrix J with Equation (7).

Step 3. Solve for the Newton direction $\Delta\omega_{i,r}^k \leftarrow -\alpha_1 J^{-1} g^S$ ($i = 1, \ldots, N_c$ and $r = 1, \ldots, N_r$) where α_1 is a user-defined under-relaxation coefficient.

Step 4. Calculate the under-relaxation coefficient necessary to enforce the minimum molar volume constraint

$$\alpha_2 = \min_{r=1,\ldots,N_r} \left\{ \gamma_2 \frac{V_r - \sum_{i=1}^{N_c} b_i n_{i,r}}{\sum_{i=1}^{N_c} b_i n_i \Delta\omega_{i,r}^k} \text{ if } \sum_{i=1}^{N_c} b_i n_i \Delta\omega_{i,r}^k > 0, 1 \right\} \tag{10}$$

Step 5. Calculate the under-relaxation coefficient necessary to enforce the minimum number of moles constraint

$$\alpha_3 = \min_{\substack{r=1,\ldots,N_r \\ i=1,\ldots,N_c}} \left\{ -\gamma_2 \frac{\omega_{i,r}}{\Delta\omega_{i,r}^k \alpha_2} \text{ if } \Delta\omega_{i,r}^k < 0, 1 \right\} \tag{11}$$

Step 6. Update the independent variables $\omega_{i,r}^k \leftarrow \omega_{i,r}^{k-1} + \alpha_2\alpha_3\Delta\omega_{i,r}^k$ where $i = 1, \ldots, N_c$ and $r = 1, \ldots, N_r$. Set $\omega_{i,N_r}^k \leftarrow \omega_{i,N_r}^{k-1} - \alpha_2\alpha_3 \sum_{r=1}^{N_r-1} \Delta\omega_{i,r}^k$ where $i = 1, \ldots, N_c$.

Step 7. Check for convergence. If $||g^S||_\infty \le \varepsilon_{MPTA}$, then stop. Otherwise, set $k \leftarrow k+1$. In this research, ε_{MPTA} is 10^{-10}.

In Step 3, α_1 is an underrelaxation parameter which is set to 0.5 if $||g^S||_\infty > 10^{-2}$ and $N_r = 100$. When $N_r = 2$, α is set to 1. γ_2 is the user-defined parameter that should be set to a value less than 1. All the calculations presented in this paper use $\gamma_2 = 0.8$.

2.3. Implementation in a flow simulator

This section explains the methodology for approximating the 100-region MPTA calculation with a 2-region MPTA calculation to account for the density distribution across the pore when computing the fluxes in the reservoir simulation. Fig. 1 schematically summarizes the process of this approximation.

First, the 100-region MPTA calculation computes the composition and density distribution at a constant temperature, total pore volume, and number of moles of each component. Fig. 1b shows a schematic for a molar density ρ distribution across a pore as a function of z. The horizontal dashed line represents the molar density at the center of the pore ρ_0. The number of bulk moles n^b per mass of solid rock m^s is $\frac{n^b}{m^s} = \rho_0 z_0$,

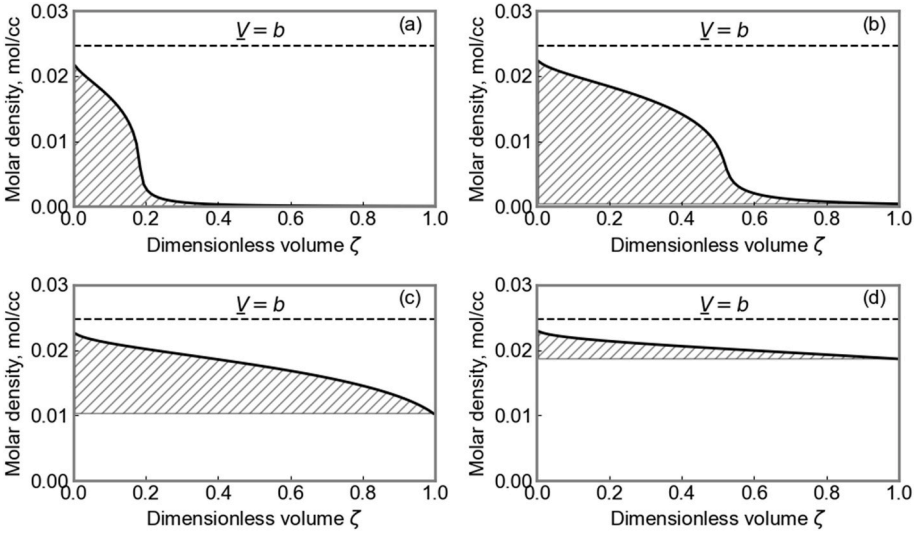

Fig. 2. Density distribution in the pore calculated using the MPTA calculation for pure ethane at 323 K and a bulk pressure of (a) 1 bar, (b) 10 bar, (c) 100 bar, and (d) 1000 bar. In each plot, the shaded area represents the area integrated to calculate the number of excess moles and the dashed one represents the physical maximum molar density where there would be no more empty space between molecules.

which represents the number of moles in the pore if there is no interaction with the pore wall and the density is uniformly equal to ρ_0. The pressure evaluated at the composition and density at the center of the pore is called the bulk pressure P^b. The number of excess moles n^{ex} per mass of solid rock m^s is equal to the shaded area between the ρ curve and the ρ_0 dashed line

$$\frac{n^{ex}}{m^s} = \int_0^{z_0} (\rho - \rho_0) dz. \tag{12}$$

The number of excess moles represents the additional number of moles present in the pore because of the interactions with the pore wall.

The next step is to split the pore into a central and a sorbed layer such that the sorbed layer is the volume adjacent to the pore wall which contains most of the excess moles. The vertical dashed line in Fig. 1b creates a sorbed layer with a volume fraction S_S and a central layer volume fraction $S_C = 1 - S_S$. Fig. 1c shows the average density for both layers. Fig. 1d schematically shows the geometry of these two concentric layers in the pore. Note that the density in the central layer is close to, but not equal to ρ_0 in Fig. 1c.

In the simulation in this research, the densities and compositions of both layers are approximated by a 2-region MPTA calculation at a fixed sorbed layer volume fraction to accelerate the calculation. In this 2-region approximation, the sorbed and central layers are the region adjacent to the pore wall and the central region of the pore, respectively.

The in-house simulator, TigReS, uses the Dusty Gas Model (DGM) (Achour and Okuno, 2022) to compute the diffusion coefficients in both layers as a function of the density and composition of each layer. The mole balance is solved using a partially implicit method, where only the fugacities and mole numbers are treated implicitly in the mole balance equation

$$\boldsymbol{n}^{t+1} - \boldsymbol{n}^t - \boldsymbol{R}_C^t \boldsymbol{f}_C^{t+1} - \boldsymbol{Q}_C^t - \boldsymbol{R}_S^t \boldsymbol{f}_S^{t+1} = \boldsymbol{0}. \tag{13}$$

In Equation (13), t is the time step index, $\boldsymbol{n}$ is the vector containing the total number of moles in each grid block for each component, and $\boldsymbol{f}$ is the vector containing the fugacities of each component in each grid block, $\boldsymbol{R}$ is the transmissibility matrix containing DGM diffusion coefficients, and $\boldsymbol{Q}$ is the vector containing the boundary condition information as described by Achour and Okuno (2022). The subscripts C and S represent the central and sorbed layers, respectively.

The transmissibility coefficient matrix accounts for the presence of multiple phases and layers by using the saturation-weighted sum of diffusion coefficients and multiplying by the layer volume fraction. The transmissibility between the grid blocks k and $k-1$ for layer L is

$$R_L^{k-\frac{1}{2}} = S_L \left(\sum_{j=1}^{N_p} \mathcal{D}_{j,L} S_{j,L} \right)^{k-1/2} \frac{2A_k A_{k-1}}{\Delta x_k A_{k-1} + \Delta x_{k-1} A_k} \tag{14}$$

where S_L is the L ($L = C, S$) layer volume fraction, $\mathcal{D}_{j,L}$ and S_{jL} are the upwinded diffusion coefficient matrix and saturations for phase j within layer L, and A_k A_{k-1} Δx_k Δx_{k-1} are the cross-sectional area and lengths of grid blocks k and k-1. TigReS calculates the upwinded diffusion coefficients and phase saturations based on the sum of fugacities where

- $\left(\sum_{j=1}^{N_p} \mathcal{D}_{j,L} S_{j,L} \right)^{k-1/2} = \left(\sum_{j=1}^{N_p} \mathcal{D}_{j,L} S_{j,L} \right)^{k}$ if $\sum_{i=1}^{N_c} f_i^k > \sum_{i=1}^{N_c} f_i^{k-1}$,
- otherwise, $\left(\sum_{j=1}^{N_p} \mathcal{D}_{j,L} S_{j,L} \right)^{k-1\backslash 2} = \left(\sum_{j=1}^{N_p} \mathcal{D}_{j,L} S_{j,L} \right)^{k-1}$.

3. Case studies

This section demonstrates the practical advantages of the algorithms developed in this research. Case 1 provides a general overview of our MPTA algorithm by explaining how it computes the number of excess moles, benchmarking with another paper's calculations for pure ethane. It also presents the computational efficiency of using the 2-region MPTA. Case 2 compares the calculation of ethane excess moles with ML and MPTA. Case 3 shows example calculations for 2 and 100 regions with a ternary mixture and explains how to select an optimal sorbed layer volume fraction for flow simulation. Case 4 shows an example simulation of diffusion for the same ternary mixture as in case 3 with and without capillary pressure and sorption.

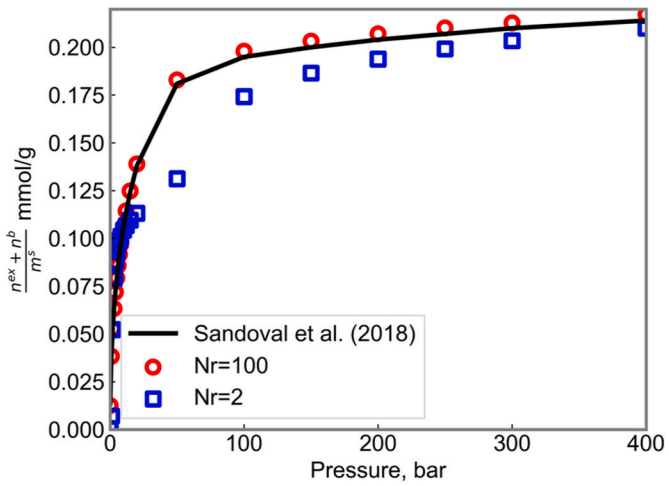

Fig. 3. Comparison of the MPTA calculation by Sandoval et al. (2018) for pure ethane at 323 K and the MPTA algorithm used in this paper with Nr = 100 and Nr = 2.

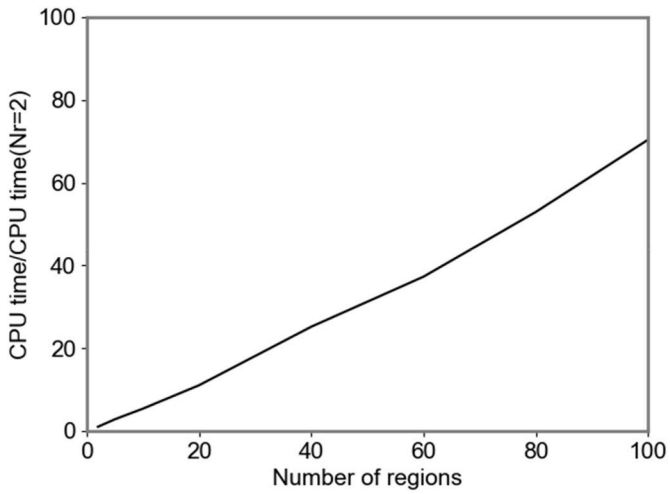

Fig. 4. Ratio of the computational times with various Nr values to the computational time with Nr = 2 for MPTA calculations at the bulk pressure data points in Fig. 3.

3.1. Case 1

This subsection first explains how the MPTA method calculates the number of excess moles, and then it benchmarks the excess moles calculated for pure ethane with the data in the literature. It shows that using only 2 regions can accelerate the calculation while keeping a reasonable level of accuracy for a pure ethane fluid.

Wang et al. (2015) reported the experimentally measured number of excess moles for the measured porosity of $\varphi = 3.1\%$. Sandoval et al. (2018) fitted Wang et al.'s sorption data with the MPTA method with the parameters $\beta = 1.02$, $\varepsilon/R = 724.8\,K^{-1}$, and $z_0 = 11.23\,mm^3/g$ in their supporting information. The critical temperature, pressure, and acentric factor of ethane are 305.3 K, 48.72 bar, and 0.0995, respectively.

Fig. 2 shows the density distribution computed using a 100-region MPTA calculation as a function of dimensionless volume from the pore wall ζ at 323 K and a bulk pressure P^b of (a) 1 bar, (b) 10 bar, (c) 100 bar, and (d) 1000 bar. Each region in the 100-region calculation contains 1% of the pore volume and each region in the 2-region calculation contains 50% of the pore volume. The shaded area represents the number of excess moles n^{ex} per mass of solid rock m^s. In Fig. 2, the dashed line indicates the density at which $\underline{V} = b$, where $\underline{V}$ and b are respectively the molar volume and the co-volume parameter for the cubic equation of state. Physically, b represents the molar volume at which the molecules are packed so close together that there is no more free space.

Ocular inspection of the density profiles suggests the existence of a sorbed layer containing the majority of the excess moles occupying about 20% of the pore volume at 1 bar and 50% at 10 bar. Note that the increase in density is not caused by a phase transition since the temperature is greater than the critical temperature of ethane. At 100 and 1000 bars, it is harder to visually identify a sorbed layer. Hence, a mathematical definition will be presented in section 3.3 to split the pore into a central and sorbed layer at all pressures.

Another subtle observation is that the number of excess moles represented by the shaded area increases from 1 to 10 bars but decreases from 10 to 100–1000 bar. This is because the bulk density ρ_0 approaches the dashed line as the bulk pressure P^b increases. This decreases the range of density values that can span the density distribution from the pore center to the wall. Consequently, the number of excess moles tends to decrease with increasing pressure. At the limit of infinite pressure, the density profile will reach the dashed line; that is,

$$\lim_{P^b \to \infty} n^{ex} = 0. \tag{15}$$

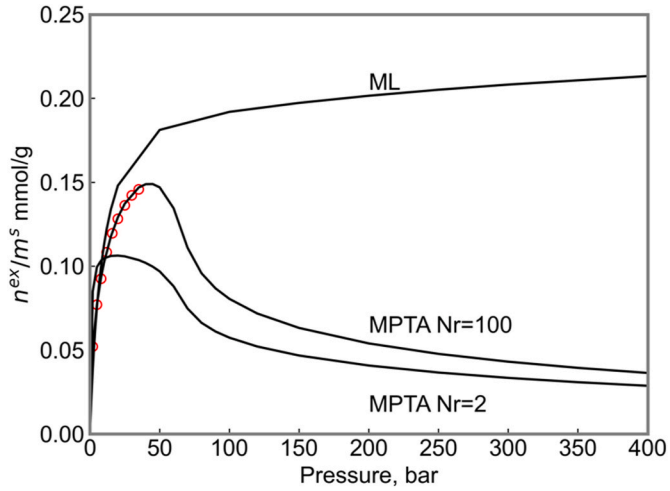

Fig. 5. Comparison of the number of excess moles calculated by ML and MPTA with Nr = 100 and Nr = 2 for pure ethane at 323 K. Experimentally measured values are shown by hollow circles.

The maximum molar density of a multicomponent mixture is a function of the local composition and would not form a straight line like the dashed lines in Fig. 2. As will be shown in section 3.3, the number of excess moles is a decreasing function of pressure at high pressures even for multicomponent mixtures.

In Fig. 3, the bold line shows the sum of the excess moles n^{ex} and bulk n^b moles per mass of solid rock m^s calculated by the MPTA implementation of Sandoval et al. (2018). The hollow circles and squares are calculated by the algorithm presented in this paper using 100 and 2 equivolume regions, respectively. The comparison of the numerical solution of our 100-region MPTA with Sandoval et al. (2018) shows good agreement. Also, the 2-region calculation reasonably approximates the 100-region calculation at high bulk pressures, although it underestimates at low bulk pressures. This underestimation comes with a substantially reduced computational cost of the MPTA calculation as described below.

Fig. 4 shows the computational time for calculating all the data points in Fig. 3 with different numbers of regions in the x-axis divided by the computational time with 2 regions (i.e., pure ethane at 323 K). The

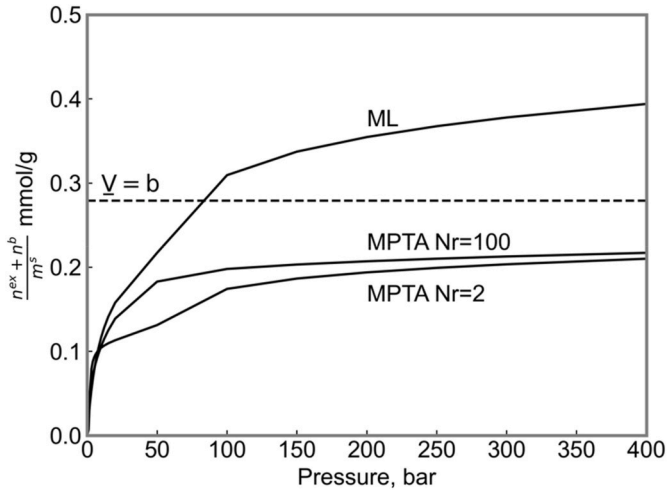

Fig. 6. Comparison of the sum of ML, and MPTA with Nr = 100 and Nr = 2 for pure Ethane at 323 K.

computational time of this calculation is dominated by the stability analysis (Achour and Okuno, 2020) in each region as part of Step 1 in Section 2.2. This figure shows that the 2-region MPTA is about 70 times faster than the 100-region MPTA.

3.2. Case 2

This case compares the multicomponent sorption calculation of MPTA and ML for pure ethane at 323 K calibrated for a Marcellus shale sample. This case is based on the same dataset as the one used in case 1. Sandoval et al. (2018) calibrated an ML model

$$\frac{n^{ex}}{m^s} = n_{max}\frac{bf}{1+bf} \tag{16}$$

for the same experimental data as the MPTA model in case 1 with the parameters $n_{max} = 0.234$ mmol/g, $b = 0.0986\ bar^{-1}$, and where f is the fugacity of ethane.

Fig. 5 shows the number of excess moles n^{ex} per mass of solid rock m^s as predicted by ML, the 100-region and 2-region MPTA calculation, and the experimentally measured values with hollow circles. Although the ML fits the experimental data and 100-region MPTA at low bulk pressures, it significantly deviates from the 100-region MPTA calculation at high bulk pressures because ML is always a monotonically increasing function with bulk pressure. As explained in section 3.1, the number of excess moles is expected to be non-monotonic and converge to 0 at high bulk pressures for pure substances. That is, ML is fundamentally inaccurate for predicting the number of excess moles at reservoir pressures. The 2-region MPTA is also non-monotonic, although it is not accurate at low bulk pressures. At high bulk pressures, however, it converges to the value predicted by Nr = 100.

Fig. 6 shows the sum of the bulk moles n^b calculated by the equation of state and the excess moles n^{ex} from Fig. 5 per mass of solid rock m^s.

Table 2
Reservoir and fluid properties used to calculate the capillary pressure in case 3.

k	φ	τ	T	P	r	γ	z_0	β
mD			K	bar	nm		mmol/g	
$2. \times 10^{-4}$	10%	33	390	100	8	3.88	11.23	1.02

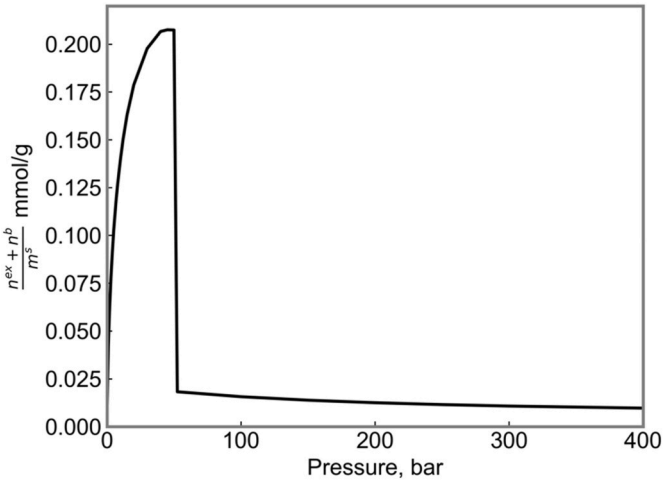

Fig. 7. Comparison of the number of excess mole per mass of solid rock calculated by ML and MPTA with Nr = 100 and Nr = 2 for pure Ethane at 323 K. Experimentally measured values are shown by hollow circles.

The dashed line indicates the number of moles in the pore volume at which $\underline{V} = b$, where $\underline{V}$ and b are the molar volume and the co-volume parameter given by the cubic equation of state, respectively. Although ML approximates the MPTA prediction well at low bulk pressures, it deviates significantly at high bulk pressures and exceeds the maximum density line $\underline{V} = b$. This means that the sorbed layer density is calculated to be greater than the maximum density for ethane; this re-confirms the inaccuracy of ML at high bulk pressures. Consequently, transport coefficient models cannot be used to compute the transport coefficients for the sorbed layer since the density is outside the range of values that they are calibrated for. On the other hand, the Nr = 2 line systematically underestimates the MPTA Nr = 100 line on average by 0.017 mmol/g. However, it approaches the Nr = 100 line at high bulk pressures and is fundamentally guaranteed to not exceed the $\underline{V} = b$ line because it is subject to Equation (5).

Careful investigation of the literature shows that the number of excess moles is a decreasing function of pressure at higher bulk pressure even for pure substances predicted by molecular dynamics simulation and experimental measurements (Jin, 2018; Baek and Akkutlu, 2019; Gong et al., 2020; Clarkson and Haghshenas, 2013; Barsotti et al., 2016; Huang et al., 2018). The most common description of this phenomenon appears to be that molecules tend to start desorbing from the surface at higher pressure when the substance becomes supercritical (Klewiah et al., 2020). To the authors' knowledge, no thorough analysis has yet

Table 1
Parameters for the PR EOS, MPTA, interfacial tension, and viscosity used in case 3.

	Tc	Pc	ω	$\underline{V}c$	MWt	ε/R	Parachor	BIP		
	K	Bar		cc/mol	g/mol	K^{-1}		C_1	nC_4	nC_{10}
C_1	190.6	46.60	0.008	99.0	16.04	506.6	74.05	0	0	0.0422
nC_4	425.2	38.00	0.193	255.0	58.12	1161.2	193.9	0	0	0.0078
nC_{10}	605.5	23.60	0.463	574.0	134.0	2470.3	440.69	0.0422	0.0078	0

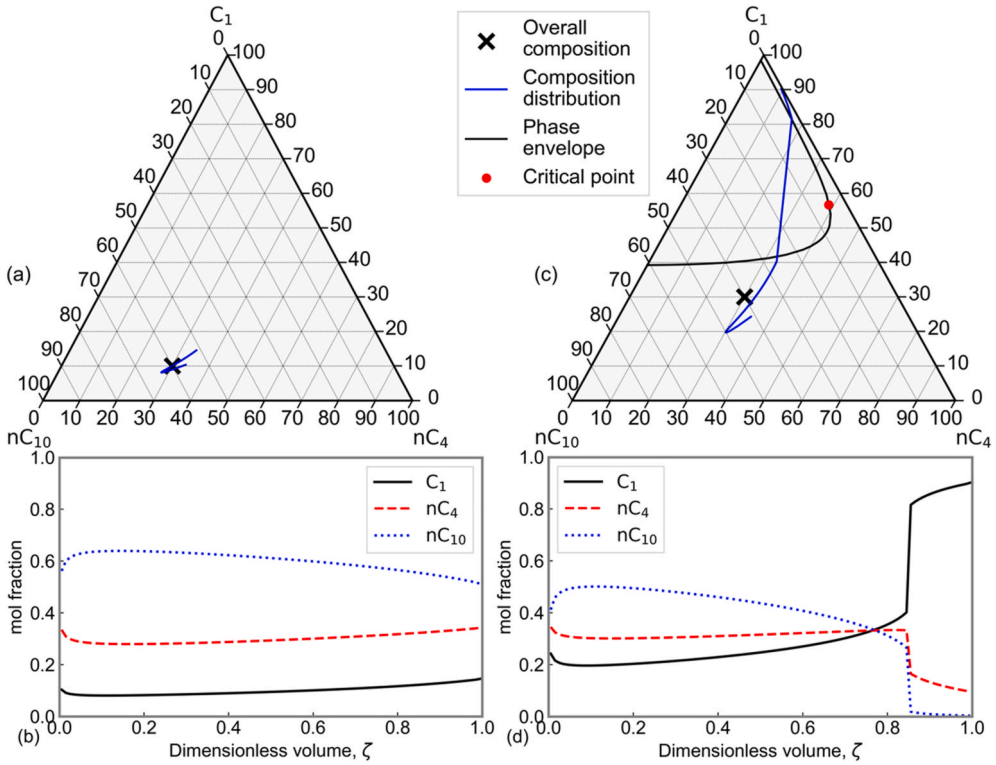

Fig. 8. Composition profiles across a Marcellus shale pore at 390 K and 100 bar calculated with MPTA and the Young-Laplace capillary pressure for two 8-nm pores containing a mixture of (a) (b) 10% C_1 30% nC_4 and 60% nC_{10}, and a mixture of (c) (d) C_1 30% C_1 30% nC_4 and 40% C_{10}. The phase envelope at 139 bar includes the effect of capillary pressure.

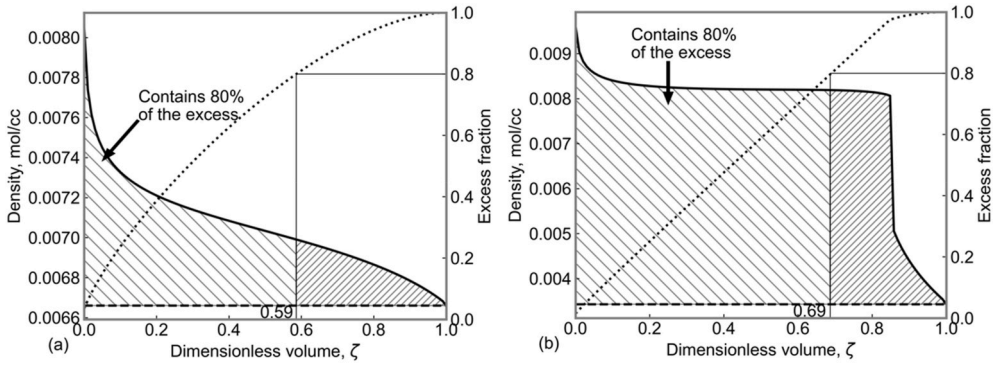

Fig. 9. Density profiles across a Marcellus shale pore at 390 K and 100 bar calculated with MPTA and the Young-Laplace capillary pressure for an 8 nm pore containing (a) 10% C_1, 30% nC_4, and 60% C_{10}, and (b) 30% C_1, 30% nC_4, and 40% C_{10}. The dotted line represents the normalized integral of the difference between the density and the density at the center of the pore.

explained why the number of excess moles must decrease at a high bulk pressure. The fundamental reason, which has not been explained in the literature, is simply that the density at the pore center ρ^b must tend to its maximum value across the pore with increasing bulk pressure, as shown in section 3.1. The physical inconstancy of the monotonically increasing ML at high bulk pressure has never been carefully explained likely because sorption is only measured at low bulk pressures with light gases where experimental measurements and ML are generally accurate.

3.3. Case 3

This case compares the accuracy of the 2-region approximation with a full MPTA calculation and demonstrates the method for determining the sorbed layer volume fraction for a ternary mixture of methane (C_1), n-butane (nC_4), and n-decane (nC_{10}) at 390 K and 100 bar. Table 1 shows the critical temperature Tc, the critical pressure Pc, the acentric factor ω, the critical volume Vc, the molecular weight MWt, the DRA wall potential parameter divided by the universal gas constant R taken from Sandoval et al. (2018), the parachor parameters, and the binary interaction parameters (BIP). Table 2 shows the reservoir properties used for this case including the parachor exponent γ, and the DRA parameters z_0 and β. The pore size and permeability were taken from Milliken et al. (2013) and the tortuosity was calculated using the Carman-Kozeny relationship (Peters, 2012) $\tau = \varphi r_H^2/2k$, where φ, k, and r_H are porosity, permeability, and hydraulic radius approximated as the average pore radius r. DRA parameters were taken from Sandoval et al. (2018). The pore size and parachor model for the interfacial tension

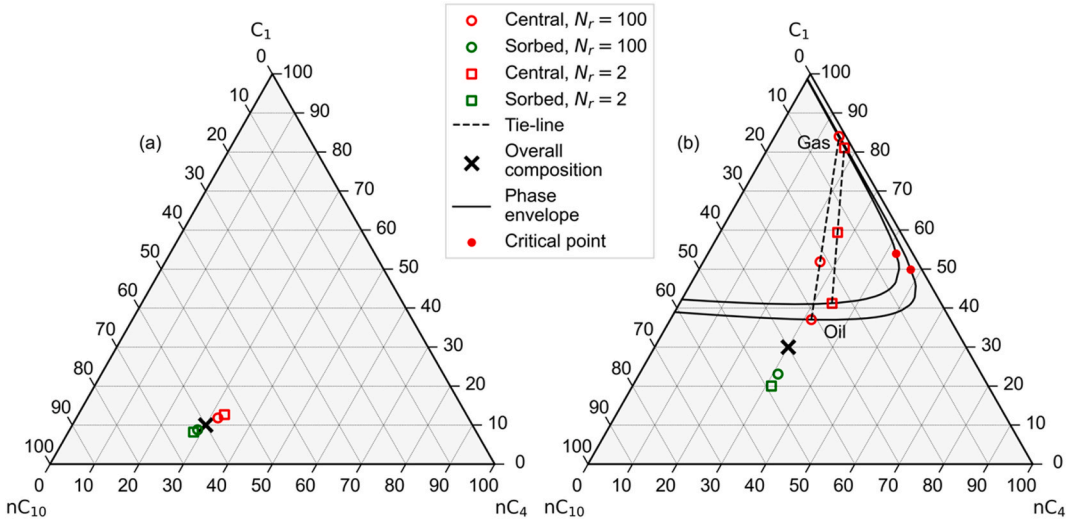

Fig. 10. Mole fraction distribution profiles across a Marcellus shale pore at 390 K and 100 bar calculated with MPTA and the Young-Laplace capillary pressure for an 8-nm pore containing (a) 10% C_1, 30% nC_4, and 60% nC_{10} and (b) 30% C_1, 30% nC_4, and 40% nC_{10}. The black cross, hollow circles, and hollow squares represent the overall compositions of the pore, and the layer compositions calculated using 100 and two regions, respectively. The phase envelopes have been calculated at an oil pressure of 110 bar for the 100-region central layer and 126 bar for the 2-region central layer.

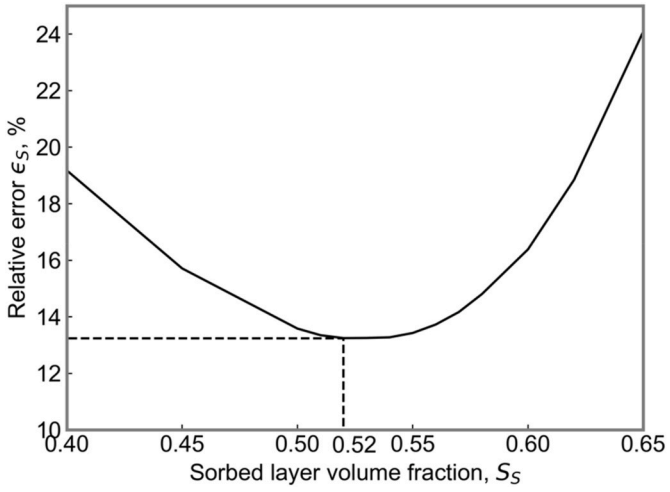

Fig. 11. Average deviation in layer compositions and molar volume calculations between 2 and 100 regions uniformly distributed samples in composition space as a function of the fixed sorbed layer volume fraction for the 2-region MPTA.

were used to compute the capillary pressure based on the Young-Laplace model.

Fig. 7 shows the excess moles for a mixture of 10% C_1, 30% nC_4, and 60% nC_{10} as a function of bulk pressure. The number of excess moles drops at 50 bar because the phase transition from gas to oil occurs at the pore center. The main purpose of this plot is to provide further evidence that the number of excess moles is a decreasing function of bulk pressure at high bulk pressures even for multicomponent mixtures as shown for pure substances in sections 3.1 and 3.2.

Fig. 8ab show the composition distribution calculated using 100 discrete regions for a pore containing 10% C_1, 30% nC_4, and 60% C_{10}. Fig. 8cd show them for 30% C_1, 30% nC_4, and 40% C_{10}. On the ternary diagrams (Fig. 8ac), the overall composition is represented by a cross. For reference, Fig. 8c includes the phase envelope at 139 bar and 390 K and a tie-line which separates the fluid compositions near the pore center and the pore wall. For both mixtures, lighter and heavy components appear to segregate from the pore center to the pore wall. At the pore wall, this trend reverses for a very small fraction of pore volume. This reversal is also observable in Fig. 8a and c.

Fig. 9 shows the density distribution for a pore containing (a) 10% C_1, 30% nC_4, and 60% C_{10} and (b) 30% C_1, 30% nC_4, and 40% C_{10}. The dotted line shows the excess fraction, which is the fraction of the excess moles contained in the sorbed layer $0 < \zeta < S_S$; that is,

$$\frac{n_S^{ex}(S_S)}{n^{ex}} = \int_0^{S_S} (\rho - \rho_0) d\zeta \Big/ \int_0^1 (\rho - \rho_0) d\zeta. \tag{17}$$

To split the pore into a central and sorbed layer, we define the sorbed layer such that it contains 80% of the total sorbed amount. The resulting sorbed layer volume fractions are 59% for Fig. 9a and 69% for Fig. 9b. The compositions of the sorbed and central layers are shown in Fig. 10 with hollow green and red circles. The central layer of the second mixture (Fig. 10b) splits into two phases at equilibrium as labeled as oil and gas. The calculation was repeated with 2 regions using 59% and 69% sorbed layer volume fractions with the same overall compositions and volumes as for the 100-region calculation. The compositions of both layers are shown with hollow squares. The 2-region calculation is shown to reasonably approximate the compositions of the central and sorbed layers for both cases.

Fig. 11 shows the average deviation of layer composition and molar volume over the entire composition space between the 100-region calculation and the 2-region approximation as a function of the sorbed layer volume fraction used in the 2-region approximation. At each point in composition space, the sorbed layer volume fraction is fixed at S_S for $N_r = 2$ while it is determined based on the 80% threshold condition for the 100-region calculation. The deviation is calculated as the sum of deviations

$$\varepsilon_S = \frac{\sum_{Samples} \sum_{L=S,C} \left(\left| \frac{\ln(\underline{V}_{2,L}) - \ln(\underline{V}_{100,L})}{\ln(\underline{V}_{100,L})} \right| + \sum_{i=1}^{N_c} \left| \frac{\ln(x_{i,L,2}) - \ln(x_{i,L,100})}{\ln(x_{i,L,100})} \right| \right)}{2N(N_c + 1)} \tag{18}$$

for $N = 66$ uniformly distributed sample points in composition space and both layers. The first, second, and third subscripts of the component mole fraction x denote the component index, the layer index, and the number of regions used in the MPTA calculation. The first and second subscripts of molar volume $\underline{V}$ represent the number of regions used in the MPTA calculation and the layer index. The deviation of the loga-

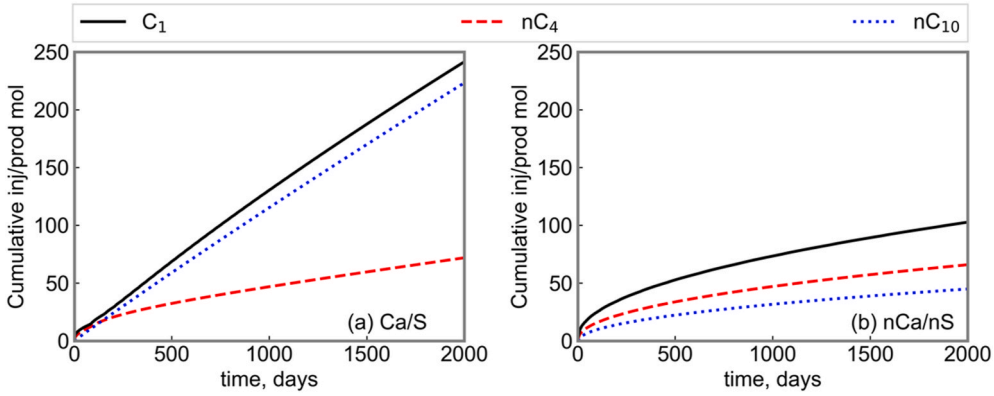

Fig. 12. Cumulative moles recovered and injected for 2 years of continuous diffusion of methane into a Marcellus shale reservoir containing a mixture of 30% n-butane and 70% n-decane (a) with capillary pressure and sorption, (b) without capillary pressure and sorption. Bold, dashed, and dotted lines represented injected methane and produced n-butane and n-decane, respectively.

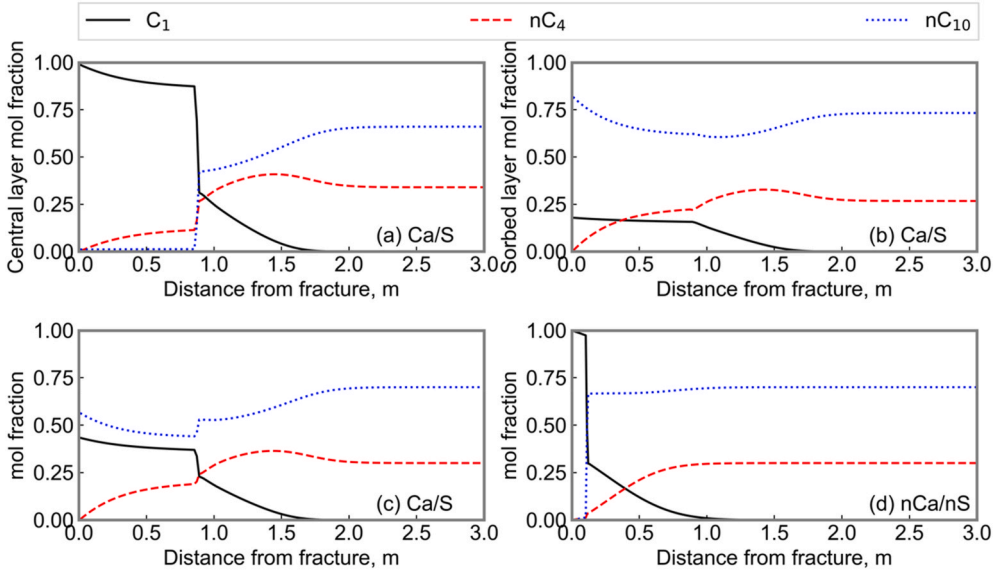

Fig. 13. Mol fraction profile after 2 years of continuous methane injection into a Marcellus shale containing a mixture of 30% n-butane and 70% n-decane including both capillary pressure and sorption (a) for the central layer, (b) for the sorbed layer and (c) overall, and (d) excluding capillary pressure and sorption. Bold, dashed, and dotted lines represented injected methane and produced n-butane and n-decane, respectively.

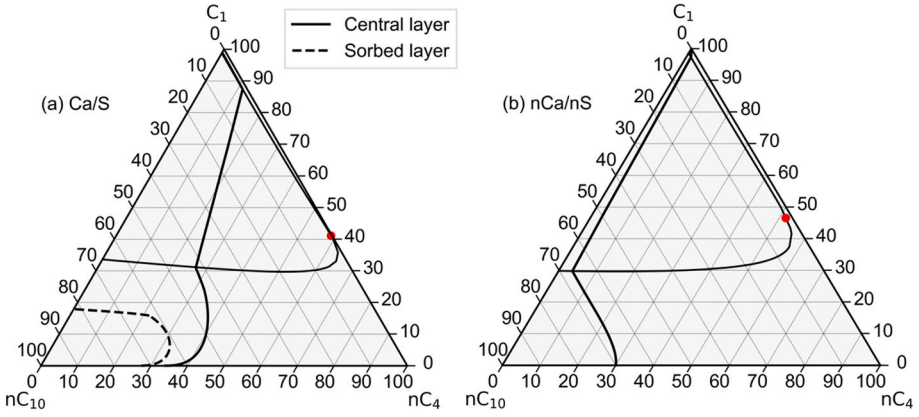

Fig. 14. Composition route after 2000 days of continuous methane injection into a Marcellus shale containing a mixture of 30% n-butane and 70% n-decane including (a) both capillary pressure and sorption, and (b) excluding capillary pressure and sorption. On (a), the bulk and sorbed layer composition routes are shown with a bold and dashed line, respectively. Phase envelopes are drawn with a red circle for a critical point for oil pressures of (a) 84.26 bar and (b) 100.05 bar. Lines in the two-phase zone for (a) and (b) are tie-lines.

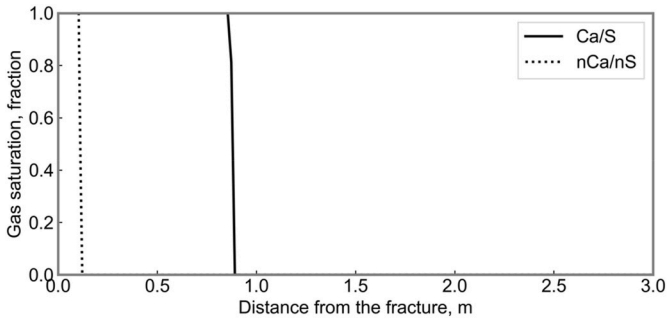

Fig. 15. Gas saturation profile after 2 years of continuous methane injection into a Marcellus shale containing a mixture of 30% n-butane and 70% n-decane including both capillary pressure and sorption with a bold line and excluding capillary pressure and sorption with a dotted line. The Ca/S plot shows the gas saturation profile of the central layer since the sorbed layer remains liquid.

rithm of x and $\underline{V}$ is used to decrease the effect of the different levels of variability in the molar volume and composition. The deviation at the minimum between the 2- and 100-region calculations is about 13% for a sorbed layer volume fraction of 52%.

The relative error plot is expected to produce a convex shape, as shown in Fig. 11, to identify an optimal sorbed layer volume fraction. The relative error for each term in the sum of Equation (18) increases with the difference between the sorbed layer volume fraction for the 2-region calculation and that determined by the threshold criterion in the 100-region calculation. Since each sample point in composition space has a different sorbed layer volume fraction, Equation (18) essentially acts as a proxy variable for the average difference between the threshold-based sorbed layer volume fraction and the x-axis in Fig. 11. The minimum of ε_S is then at an average of the S_S for the 100-region calculations with the 80% threshold. Appendix B shows a flowchart that describes the process of calculating the deviation ε_S as a function of S_S in the 2-region approximation.

3.4. Case 4

This case presents a simulation case of diffusion through the central and sorbed layers when methane is transported into a tight porous medium based on the Marcellus shale data. The initial composition is assumed as a binary mixture of 30 mol% n-butane and 70 mol% n-decane. The EOS, MPTA, and Lohrenz et al. (1964) viscosity parameters for this mixture are given in Table 1. The reservoir properties are shown in Table 2. The total reservoir length is 9 m for all cases. Note that the simulation in this subsection uses two-region MPTA, and the two regions are the central and sorbed layers.

Since capillary pressure and sorption are fully coupled in the compositional transport, we focus on the comparison between two simulations using TigRes, Ca/S and nCa/nS; "Ca/S" refers to the simulation including the effects of both sorption and capillary pressure using 500 grid blocks and "nCa/nS" refers to the simulation without the effects of capillary pressure or sorption using 1000 grid blocks. The number of grid blocks for each case has been determined by gradually increasing it until the calculated results stopped changing. For all simulations, pure methane is the fracture fluid composition, and the initial reservoir pressure and the boundary pressure are set to 100 bar. In the Ca/S simulation, the pressure of the central layer is set to 100 bar.

Fig. 12 shows the injected and produced moles (a: Ca/S) with capillary pressure and sorption, and (b: nCa/nS) without capillary pressure and sorption. In this figure, the main difference between the two simulations lies in the rates of methane injection (the lightest component) and n-decane production (the heaviest component). That is, the Ca/S simulation shows the enhanced rates of methane injection and n-decane production, in comparison to the nCa/nS simulation. This marked difference comes from the compositional segregation in the sorbed and central layers and its impact on multicomponent diffusion as explained below. Note that this enhanced transport is not because of the denser sorbed layer since the inclusion of sorption increases the number of initial oil moles in the reservoir by only 7.8%; while the enhancement shown in Fig. 12 is a factor more than two after two years.

Fig. 13 shows the mole fraction profiles for the Ca/S and nCa/nS simulations, where Fig. 13a and b give the mole fractions in the sorbed and central layers, respectively, while Fig. 13c gives the overall mole fractions for the Ca/S simulation. Fig. 13d shows the overall mole fractions in the nCa/nS simulation. Fig. 14ab depict the mole fraction profiles from the two simulations using ternary diagrams.

The central-layer composition profiles have a discontinuity near the fracture at which the central layer displays a transition from the gaseous to oleic phase as shown in Figs. 13 and 15. This transition corresponds to a jump across a tie-line with the same fugacity on both ends of this line (Fig. 14). Fig. 14 also shows the phase envelope for each simulation at the oil-phase pressure on the tie-line after 2000 days. The key difference between the Ca/S and nCa/nS simulations is in the compositional variation in the single oleic phase as can be seen in Fig. 14.

The comparison between the two simulations indicates that methane has a lower overall concentration near the fracture but reaches much deeper into the reservoir in the Ca/S simulation. Likewise, the decrease in n-decane mole fraction reaches deeper into the reservoir causing an increase in n-decane production (Fig. 12a). Fig. 13a shows that methane (the lightest component) is transported deep into the reservoir by diffusing through the center of the pore while Fig. 13b shows that n-decane (the heaviest component) is diffused primarily through the sorbed layer, especially near the fracture. However, n-butane (the intermediate component) does not show preferential partitioning into either layer, resulting in a relatively small change in the rate of mass transfer across the fracture as shown in Fig. 12. That is, the lightest and heaviest components exhibit clear segregation in the central and sorbed layers according to their relative affinity for the pore wall. The intermediate component serves as an additional degree of freedom in the segregated compositional transport in this ternary example.

The compositional segregation enhances the methane injection and n-decane production rates in the Ca/S simulation. The segregated transport increased the depth of penetration of the injected methane by 50% after 2 years as shown in Fig. 13.

Figs. 13c and 14b show that in the absence of sorption and capillary pressure, the n-decane concentration remains nearly constant (immobile) when methane and n-butane show their counter-current diffusion. Fig. 13ab and 14a show that the different affinities of methane and n-decane for the pore wall enabled their segregated counter-current transport. This highlights the clear difference in compositional transport between the two simulations, Ca/S and nCa/nS.

Tovar et al. (2021) conducted CO_2 huff-and-puff experiments with Wolfcamp shale and Berea Sandstone cores saturated with dead oil and reported the composition of the effluent oil. Table A1 in their paper shows that the weight fraction of n-decane in the produced oil from the shale core was approximately twice that of the Berea sandstone. However, the n-butane weight fraction barely changed between the shale and sandstone experiments. The difference between the two experiments is consistent with the effect of sorption on the cumulative production of n-butane and n-decane shown in Fig. 12.

4. Conclusions

This paper presented the implementation of MPTA for modeling the equilibrium and transport in the central and sorbed layers in multicomponent diffusion in tight porous media. The diffusion simulations in this research highlighted the impact of sorption and capillary pressure on multicomponent diffusion. The main conclusions are as follows:

- Simulation results showed that the sorption and capillary pressure in diffusion simulations caused the compositional segregation between the central and sorbed layers. The segregation enhanced the rates of methane injection and n-decane production in their counter-current diffusion. Methane (the lightest) is transported deep into the reservoir by diffusing through the central layer while n-decane (the heaviest) is diffused primarily through the sorbed layer. N-Butane (the intermediate) did not exhibit preferential partitioning into either layer, resulting in relatively inefficient transport. The segregated transport enhanced the diffusion rates of methane and n-decane more than twice in comparison to the simulation without sorption and capillary pressure in the case studied.
- In the absence of sorption and capillary pressure, the countercurrent diffusion occurred between methane (the lightest) and n-butane (the intermediate) while n-decane (the heaviest) remained nearly immobile. That is, whether the simulation considers the surface-fluid interactions, such as sorption and capillary pressure, can substantially affect the compositional transport (e.g., produced fluid composition) through tight porous media.
- The Multicomponent Langmuir model is inaccurate at high pressures because it predicts a monotonically increasing level of sorption with pressure, and eventually a volumetric density greater than the physically allowed limit by the size of individual molecules. The 2-region MPTA presented in this research can properly account for the non-monotonic behavior of excess moles and does not violate the maximum density constraint.
- The MPTA composition distribution using 2 regions can approximate the layer composition and molar volume calculated with 100 regions by an average deviation of 13% for a ternary mixture while accelerating the computation by a factor of 70.

Credit author statement

Sofiane H. Achour: Data curation; Formal analysis; Investigation; Methodology; Validation; Visualization; Writing – original draft, Ryosuke Okuno: Conceptualization; Formal analysis; Funding acquisition; Investigation; Methodology; Project administration; Resources; Supervision; Validation; Writing – review & editing

Declaration of competing interest

The authors declare that they have no known competing financial interests or personal relationships that could have appeared to influence the work reported in this paper.

Data availability

Data will be made available on request.

Acknowledgments

We acknowledge sponsors of the Energi Simulation Industrial Affiliate Program on Carbon Utilization and Storage (Carbon UT), and the Gas EOR Industrial Affiliate Program at the Center for Subsurface Energy and the Environment at the University of Texas at Austin. Ryosuke Okuno holds the Pioneer Corporation Faculty Fellowship in Petroleum Engineering at the University of Texas at Austin.

Appendix A. Analytical expression for the Jacobian of fugacities including capillary pressure and sorption

The derivative of the logarithm of fugacity of component i ($i = 1,\ldots,N_c$) for a single-phase system based on the Peng-Robinson equation of state with respect to the number of moles of component j ($j = 1,\ldots,N_c$) at a fixed total volume is

$$\left(\frac{\partial \ln f_i}{\partial n_j}\right)_{n_{k\neq j},V} = \frac{1}{n}\left(\frac{\delta_{i,j}}{x_i} + \left(\beta_i+\beta_j\right)F_1 + \beta_i\beta_j F_1^2 + F_7\left(\beta_i\beta_j F_3 - \alpha_{ij}F_5 + \left(\beta_i\beta_j - \theta_i\beta_j - \theta_j\beta_i\right)F_6\right)\right) \tag{A1}$$

where $\delta_{i,j}$ and n are the Kronecker delta and total number of moles. Other variables in Equation (A1) are intermediate variables defined as

$$\beta_i = \frac{b_i}{b}, \tag{A2}$$

$$\alpha_{ij} = \frac{\sqrt{a_i a_j}}{a}\left(1-k_{i,j}\right), \tag{A3}$$

$$\theta_i = \sum_{j=1}^{N_c}\frac{\sqrt{a_i a_j}\left(1-k_{ij}\right)x_j}{a}, \tag{A4}$$

$$F_1 = \frac{1}{\kappa-1}, \tag{A5}$$

$$F_2 = \frac{2}{\delta_1-\delta_2}\left(\frac{\delta_1}{\kappa+\delta_1} - \frac{\delta_2}{\kappa+\delta_2}\right), \tag{A6}$$

$$F_3 = \frac{1}{\delta_1-\delta_2}\left(\left(\frac{\delta_1}{\kappa+\delta_1}\right)^2 - \left(\frac{\delta_2}{\kappa+\delta_2}\right)^2\right), \tag{A7}$$

$$F_5 = \frac{2}{\delta_1 - \delta_2} \ln\left(\frac{\kappa + \delta_1}{\kappa + \delta_2}\right), \tag{A8}$$

$$F_6 = F_2 - F_5, \tag{A9}$$

$$F_7 = \frac{a}{bRT}, \tag{A10}$$

where $k_{i,j}$ a_i and a are the binary interaction parameter and the attraction parameters of component i and the mixture based on the van der Waals mixing rules for the Peng-Robinson equation of state. δ_1 and δ_2 are the constants equal to $1 + \sqrt{2}$ and $1 - \sqrt{2}$. The Jacobian of fugacities used to compute the Jacobian of the mol balance Equation (13) is given by the chain rule

$$\left(\frac{\partial f_i}{\partial n_j}\right)_{n_{k\neq j},V} = f_i \left(\frac{\partial \ln f_i}{\partial n_j}\right)_{n_{k\neq j},V} \tag{A11}$$

The second part of the appendix presents a derivation of the derivative of the logarithm of the fugacity for two-phase systems. This derivative must account for the mass transfer of all components between the two phases to satisfy the equilibrium condition $\boldsymbol{g}^F = \boldsymbol{0}$ where $\boldsymbol{g}^F$ is a vector containing the functions

$$g_i^F = \ln f_{ig} - \ln f_{io}, \text{where i} = 1, \ldots, N_c \tag{A12}$$

and

$$g_{N_c+1}^F = \frac{1}{RT}\left(P_g - P_o - P_{cap}\right), \tag{A13}$$

where the subscripts g and o denote the gas and oil phase respectively. That is why we first need to obtain the derivative of the number of moles in the gas phase with respect to the change in the total number of moles. Let us denote a vector $\boldsymbol{t}_j$ which contains the number of moles in phase j $t_{i,j} = n_{i,j}$ ($i = 1, \ldots, N_c$) and its volume $t_{N_c+1,j} = V_j$. For the derivative of interest, the total volume is constant therefore $dt_{N_c+1o} = -dt_{N_c+1g}$. Furthermore, let us denote the net change of moles as $d\boldsymbol{n}_g$ is equal to the first Nc elements of $d\boldsymbol{t}_o + d\boldsymbol{t}_g$ and the net moles and volume transfer (MVT) from the oleic to the gaseous phase as $d\boldsymbol{t}_g^{MVT} = -d\boldsymbol{t}_o$. The differential change in $\boldsymbol{g}^F$ is then

$$d\boldsymbol{g}^F = \frac{\partial \boldsymbol{g}^F}{\partial \boldsymbol{t}_g} d\boldsymbol{t}_g + \frac{\partial \boldsymbol{g}^F}{\partial \boldsymbol{t}_o} d\boldsymbol{t}_o = \left(\frac{\partial \boldsymbol{g}^F}{\partial \boldsymbol{t}_g} - \frac{\partial \boldsymbol{g}^F}{\partial \boldsymbol{t}_o}\right) d\boldsymbol{t}_g^{MVT} + \frac{\partial \boldsymbol{g}^F}{\partial \boldsymbol{n}_g} d\boldsymbol{n}_g. \tag{A14}$$

In Equation (A14), the $\frac{\partial \boldsymbol{g}^F}{\partial \boldsymbol{n}_g}$ is a $(N_c + 1) \times N_c$ matrix, where the first N_c rows and N_c columns of $\frac{\partial \boldsymbol{g}^F}{\partial \boldsymbol{n}_g}$ are equal to Equation (A1), and the Nc+1 row is equal to

$$\frac{\partial g_{N_c+1}^F}{\partial n_{i,g}} = \frac{1}{RT}\left(\frac{\partial P_g}{\partial n_{i,g}}\right)_{n_{j,g},V_g} = \frac{1}{nb^2}\left(\frac{F_7}{\kappa^2}(F_2 - F_3) - F_1^2\right), \tag{A15}$$

where i = 1,...,N$_C$ and $\kappa = \underline{V}/b$. The derivatives of $\boldsymbol{g}^F$ with vector $\boldsymbol{t}$ is a $(N_c + 1) \times (N_c + 1)$ matrix containing 4 separate blocks

$$\frac{\partial \boldsymbol{g}^F}{\partial \boldsymbol{t}_g} - \frac{\partial \boldsymbol{g}^F}{\partial \boldsymbol{t}_o} = \left(\frac{\partial \boldsymbol{g}^F}{\partial \boldsymbol{t}_g^{MVT}}\right) = \begin{pmatrix} \boldsymbol{Q} & \boldsymbol{u} \\ \boldsymbol{v}^T & s \end{pmatrix}, \tag{A16}$$

where $\boldsymbol{Q}$ is a $N_c \times N_c$ matrix consisting of

$$Q_{ij} = \frac{\partial \ln f_i}{\partial n_{j,g}} + \frac{\partial \ln f_i}{\partial n_{j,o}}, \tag{A17}$$

where i=1,…,N$_C$ and j=1,…,N$_C$. $\boldsymbol{v}$ is a vector consisting of

$$v_i = \frac{1}{RT}\left(\frac{\partial P_g}{\partial n_{i,g}} + \frac{\partial P_o}{\partial n_{i,o}} - \frac{\partial P_{cap}}{\partial n_{i,g}} - \frac{\partial P_{cap}}{\partial n_{i,o}}\right), \tag{A18}$$

where i=1,...,N$_C$. $\boldsymbol{u}$ is a vector consisting of

$$u_i = \frac{1}{RT}\left(\frac{\partial P_g}{\partial n_{i,g}} + \frac{\partial P_o}{\partial n_{i,o}}\right), \text{where } i = 1, \ldots, N_c. \tag{A19}$$

s is a scalar expressed as

$$s = \frac{1}{RT}\left(\frac{\partial P_g}{\partial V_g} + \frac{\partial P_o}{\partial V_o} - \frac{\partial P_{cap}}{\partial V_g} - \frac{\partial P_{cap}}{\partial V_o}\right), \tag{A20}$$

where i=1,...,N_C. In Equations A19 and A20, P_{cap} is the capillary pressure and its derivative depends on the specific model used in the flash calculation. For a system at equilibrium, $d\boldsymbol{g}^F = 0$, the derivative in the moles and volume transfer from the gaseous phase to the oleic phase $d\boldsymbol{t}_g^{MVT}$ with respect to a change of net moles $d\boldsymbol{n}_g$

$$\left(\frac{d\boldsymbol{t}^{MVT}}{d\boldsymbol{n}_g}\right)_{\boldsymbol{g}^F} = -\left(\frac{\partial \boldsymbol{g}^F}{\partial \boldsymbol{t}_g^{MVT}}\right)^{-1}\frac{\partial \boldsymbol{g}^F}{\partial \boldsymbol{n}_g}. \tag{A21}$$

The total derivative of the number moles and volume $\boldsymbol{t}_g$ in the gaseous phase with respect to the total number of moles at a constant $\boldsymbol{g}^F$ is then

$$\frac{d\boldsymbol{t}_g}{d\boldsymbol{n}} = \Im - \left(\frac{\partial \boldsymbol{g}^F}{\partial \boldsymbol{t}_g^{MVT}}\right)^{-1}\frac{\partial \boldsymbol{g}^F}{\partial \boldsymbol{n}_g} \tag{A22}$$

where $\Im$ is a $(N_c+1)\times N_c$ matrix which contains the identity matrix in its first N_c rows and its last row contains zeros. The derivative of the logarithm of the fugacity at a constant $\boldsymbol{g}$ is then

$$\left(\frac{\partial \ln \boldsymbol{f}}{\partial \boldsymbol{n}}\right)_{V,\boldsymbol{g}^F} = \left(\frac{\partial \ln \boldsymbol{f}_g}{\partial \boldsymbol{t}_g}\right)\left(\Im - \left(\frac{\partial \boldsymbol{g}^F}{\partial \boldsymbol{t}_g^{MVT}}\right)^{-1}\frac{\partial \boldsymbol{g}^F}{\partial \boldsymbol{n}_g}\right), \tag{A23}$$

where $\left(\frac{\partial \ln \boldsymbol{f}_g}{\partial \boldsymbol{t}_g}\right)$ is a $N_c \times (N_c+1)$ matrix where the first N_c rows contain Equation (A1) evaluated on the gas phase and the (N_c+1) row contains

$$\frac{\partial \ln f_{i,g}}{\partial t_{N_c+1,g}} = \frac{\partial \ln f_{i,g}}{\partial V_g} = -\frac{1}{RT}\left(\frac{\partial P_g}{\partial n_{i,g}}\right)_{n_{j,g},V_g}, \tag{A24}$$

where i = 1,...,N_C. The final part of this appendix presents the expression for the derivative of the logarithm of fugacity when sorption is included using a 2-region MPTA. In this part of the appendix, subscripts denote the region index for regions 1 and 2. The equilibrium solution in the 2-region MPTA is $\boldsymbol{g}^S = 0$ where the function $\boldsymbol{g}^S$ is defined in Equation (6). Let us denote the net change of moles as $d\boldsymbol{n}_{tot} = d\boldsymbol{n}_1 + d\boldsymbol{n}_2$ and the net moles transfer (MT) from region 2 to region 1 as $d\boldsymbol{n}_1^{MT} = -d\boldsymbol{n}_2$.

The differential change in $\boldsymbol{g}^S$ is then

$$d\boldsymbol{g}^S = \left(\frac{\partial \ln \boldsymbol{f}_1}{\partial \boldsymbol{n}_1}\right)_V d\boldsymbol{n}_1 + \left(\frac{\partial \ln \boldsymbol{f}_2}{\partial \boldsymbol{n}_2}\right)_V d\boldsymbol{n}_2 = \left(\left(\frac{\partial \ln \boldsymbol{f}_1}{\partial \boldsymbol{n}_1}\right)_V + \left(\frac{\partial \ln \boldsymbol{f}_2}{\partial \boldsymbol{n}_2}\right)_V\right)d\boldsymbol{n}_1^{MT} + \left(\frac{\partial \ln \boldsymbol{f}_1}{\partial \boldsymbol{n}_1}\right)_V d\boldsymbol{n}_{tot}, \tag{A25}$$

where $\left(\frac{\partial \ln \boldsymbol{f}_1}{\partial \boldsymbol{n}_1}\right)_V$ and $\left(\frac{\partial \ln \boldsymbol{f}_2}{\partial \boldsymbol{n}_2}\right)_V$ are the derivatives of the logarithm of fugacity for regions 1 and 2 respectively given by Equation (A1) or A24 depending on whether the region contains a single or two phases. Applying the equilibrium condition $\boldsymbol{g}^S = 0$ on Equation (A25) gives the derivative of the total number of moles in region 1 as

$$\frac{d\boldsymbol{n}_1}{d\boldsymbol{n}_{tot}} = \boldsymbol{I} - \left(\left(\frac{\partial \ln \boldsymbol{f}_1}{\partial \boldsymbol{n}_1}\right)_V + \left(\frac{\partial \ln \boldsymbol{f}_2}{\partial \boldsymbol{n}_2}\right)_V\right)^{-1}\left(\frac{\partial \ln \boldsymbol{f}_1}{\partial \boldsymbol{n}_1}\right)_V, \tag{A26}$$

where $\boldsymbol{I}$ is a $N_c \times N_c$ Identity matrix. Finally, Equations 1, 9, and A26 give the derivative of the logarithm of fugacity with respect to the number of moles

$$\left(\frac{\partial \ln \boldsymbol{f}_2}{\partial \boldsymbol{n}_{tot}}\right)_V = \left(\frac{\partial \ln \boldsymbol{f}_1}{\partial \boldsymbol{n}_{tot}}\right)_V = \left(\frac{\partial \ln \boldsymbol{f}_1}{\partial \boldsymbol{n}_1}\right)_V\left(\boldsymbol{I} - \left(\left(\frac{\partial \ln \boldsymbol{f}_1}{\partial \boldsymbol{n}_1}\right)_V + \left(\frac{\partial \ln \boldsymbol{f}_2}{\partial \boldsymbol{n}_2}\right)_V\right)^{-1}\left(\frac{\partial \ln \boldsymbol{f}_1}{\partial \boldsymbol{n}_1}\right)_V\right). \tag{A27}$$

Appendix B. Optimization of S_S

The following flow chart presents the procedure for estimating the deviation between the 2-region calculation and the 100-region calculation as a function of the fixed sorbed layer volume fraction $S_{S,2}$ used in the 2-region approximation. To obtain the optimal $S_{S,2}$, the following procedure is repeated at different $S_{S,2}$ until a minimum average deviation ε_S is obtained. In the second box after the "start" step, the flow chart uses the variable $\underline{V}^{guess}$ to represent an initial guess for the total molar volume of the pore which must be updated until the bulk pressure reaches the desired value. This iterative update is necessary since the algorithm presented in this paper calculates the equilibrium at fixed moles and volume and is unable to analytically solve for the bulk pressure.

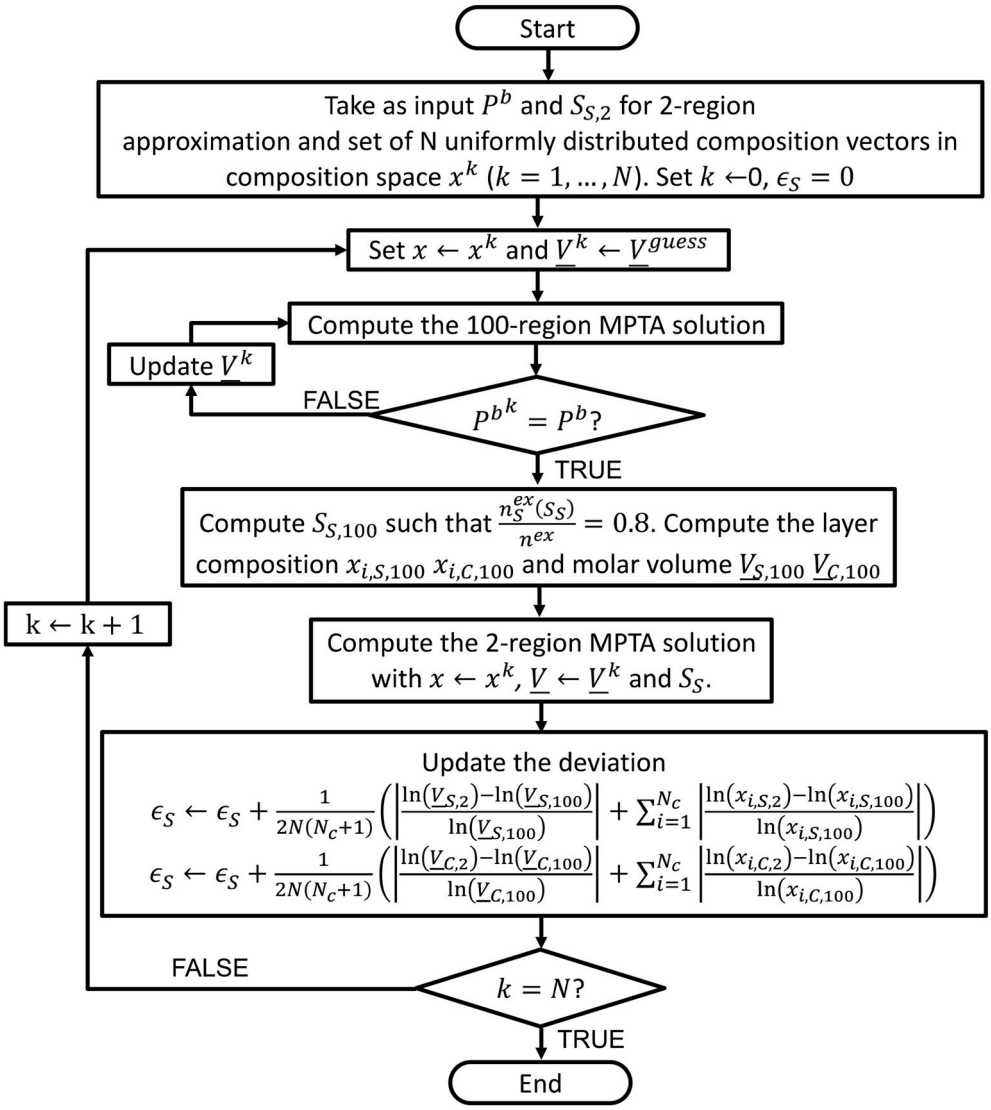

References

Achour, S.H., Okuno, R., 2020. Phase stability analysis for tight porous media by minimization of the Helmholtz free energy. Fluid Phase Equil. 520, 112648 https://doi.org/10.1016/j.fluid.2020.112648.

Achour, S.H., Okuno, R., 2021. Two-phase flash for tight porous media by minimization of the Helmholtz free energy. Fluid Phase Equil. 534, 112960 https://doi.org/10.1016/j.fluid.2021.112960.

Achour, S.H., Okuno, R., 2022. A single-phase diffusion model for gas injection in tight oil reservoirs. J. Petrol. Sci. Eng. 213, 110469 https://doi.org/10.1016/j.petrol.2022.110469.

Akkutlu, I.Y., Fathi, E., 2012. Multiscale gas transport in shales with local kerogen heterogeneities. SPE J. 17 (4), 1002–1011. https://doi.org/10.2118/146422-PA.

Baek, S., Akkutlu, I.Y., 2019. Produced-fluid composition redistribution in source rocks for hydrocarbon-in-place and thermodynamic recovery calculations. SPE J. 24 (3), 1395–1414. https://doi.org/10.2118/195578-PA.

Barsotti, E., Tan, S.P., Saraji, S., Piri, M., Chen, J.H., 2016. A review on capillary condensation in nanoporous media: implications for hydrocarbon recovery from tight reservoirs. Fuel 184, 344–361. https://doi.org/10.1016/j.fuel.2016.06.123.

Butt, H.J., Graf, K., Kappl, M., 2003. Physics and Chemistry of Interfaces. Wiley-VCH, Weineheim.

Cao, Y., 2018. Unconventional Reservoir Flow Simulation: an Improved Boundary Element Fracture Modeling Technique and the Influence of Multi-Component Diffusion/Adsorption. PhD dissertation. Texas A&M University.

Cihan, A., Tokunaga, T.K., Birkholzer, J.T., 2019. Adsorption and capillary condensation-induced imbibition in nanoporous media. Langmuir 35 (29), 9611–9621. https://doi.org/10.1021/acs.langmuir.9b00813.

Clarkson, C.R., Haghshenas, B., 2013. Modeling of supercritical fluid adsorption on organic-rich shales and coal. In: Presented at the SPE Unconventional Resources Conference, pp. 10–12. https://doi.org/10.2118/164532-MS. The Woodlands, Texas.

Computer Modelling Group (CMG), 2016. *GEM Compositional & Unconventional Reservoir Simulator*; USER GUIDE C. M.G. Ltd, Calgary, AB, Canada.

Dawass, N., D'Lima, M.L., Economou, I.G., Castier, M., 2016. Phase equilibrium with external fields: application to confined fluids. J. Chem. Eng. Data 61 (8), 2873–2885. https://doi.org/10.1021/acs.jced.6b00209.

Dubinin, M.M., 1985. Generalization of the theory of volume filling of micropores to nonhomogeneous microporous structures. Carbon 23 (4), 373–380. https://doi.org/10.1016/0008-6223(85)90029-6.

Evans, R., 1979. The nature of the liquid-vapour interface and other topics in the statistical mechanics of non-uniform, classical fluids. Adv. Phys. 28 (2), 143–200. https://doi.org/10.1080/00018737900101365.

Gherabati, S.A., Hammes, U., Male, F., Browning, J., 2018. Assessment of hydrocarbon in place and recovery factors in the eagle ford shale play. SPE Reservoir Eval. Eng. 21 (2), 291–306. https://doi.org/10.2118/189982-PA.

Gong, L., Shi, J.H., Ding, B., Huang, Z.Q., Sun, S.Y., Yao, J., 2020. Molecular insight on competitive adsorption and diffusion characteristics of shale gas in water-bearing channels. Fuel 278, 118406. https://doi.org/10.1016/j.fuel.2020.118406.

Huang, L., Ning, Z., Wang, Q., Qi, R., Zeng, Y., Qin, H., Ye, H., Zhang, W., 2018. Molecular simulation of adsorption behaviors of methane, Carbon dioxide and their mixtures on kerogen: effect of kerogen maturity and moisture content. Fuel 211, 159–172. https://doi.org/10.1016/j.fuel.2017.09.060.

Jin, Z., Firoozabadi, A., 2016. Thermodynamic modeling of phase behavior in shale media. SPE J. 21 (1), 190–207. https://doi.org/10.2118/176015-PA.

Jin, Z., 2018. Bubble/dew point and hysteresis of hydrocarbons in nanopores from molecular perspective. Fluid Phase Equil. 458, 177–185. https://doi.org/10.1016/j.fluid.2017.11.022.

Klewiah, I., Berawala, D.S., Walker, H.C.A., Andersen, P.Ø, Nadeau, P.H., 2020. Review of experimental sorption studies of CO_2 and CH_4 in shales. Journal of Natural Gas Science and Engineering 73, 103045. https://doi.org/10.1016/j.jngse.2019.103045.

Lohrenz, J., Bray, B.G., Clark, C.R., 1964. Calculating viscosities of reservoir fluids from their compositions. J. Petrol. Technol. 16 (10), 1–171. https://doi.org/10.2118/915-PA.

Ma, Y., Jamili, A., 2016. Modeling the density profiles and adsorption of pure and mixture hydrocarbons in shales. J. Unconv.Oil Gas Resour. 14, 128–138. https://doi.org/10.1016/j.juogr.2016.03.003.

Milliken, K.L., Rudnicki, M., Awwiller, D.N., Zhang, T., 2013. Organic matter-hosted pore system, Marcellus formation (devonian), Pennsylvania. AAPG Bull. 97 (2), 177–200. https://doi.org/10.1306/07231212048.

Peters, E.J., 2012. Advanced Petrophysics: Volume 1: Geology, Porosity, Absolute Permeability, Heterogeneity and Geostatistics. Live Oak Book Co, Austin, Texas.

Rangarajan, B., Lira, C.T., Subramanian, R., 1995. Simplified local density model for adsorption over large pressure ranges. AIChE J. 41 (4), 838–845. https://doi.org/10.1002/aic.690410411.

Robinson, D.B., Peng, D.Y., 1978. The Characterization of the Heptane and Heavier Fractions for GPA Peng-Robinson Programs. Gas Processors Association Research Report, Tulsa, Oklahoma.

Sandoval, D.R., Yan, W., Michelsen, M.L., Stenby, E.H., 2018. Influence of adsorption and capillary pressure on phase equilibria inside shale reservoirs. Energy Fuel. 32 (3), 2819–2833. https://doi.org/10.1021/acs.energyfuels.7b03274.

Shapiro, A.A., Stenby, E.H., 1998. Potential theory of multicomponent adsorption. J. Colloid Interface Sci. 201 (2), 146–157. https://doi.org/10.1006/jcis.1998.5424.

Shen, W., Zheng, L., Oldenburg, C.M., Cihan, A., Wan, J., Tokunaga, T.K., 2018a. Methane diffusion and adsorption in shale rocks: a numerical study using the dusty gas model in TOUGH2/EOS7C-ECBM. Transport Porous Media 123 (3), 521–531. https://doi.org/10.1007/s11242-017-0985-y.

Shen, Y., Pang, Y., Shen, Z., Tian, Y., Ge, H., 2018b. Multiparameter analysis of gas transport phenomena in shale gas reservoirs: apparent permeability characterization. Sci. Rep. 8 (1), 1–14. https://doi.org/10.1038/s41598-018-20949-2.

Tovar, F.D., Barrufet, M.A., Schechter, D.S., 2021. Enhanced oil recovery in the Wolfcamp shale by Carbon dioxide or nitrogen injection: an experimental investigation. SPE J. 26 (1), 515–537. https://doi.org/10.2118/204230-PA.

Wang, Y., Tsotsis, T.T., Jessen, K., 2015. Competitive sorption of methane/ethane mixtures on shale: measurements and modeling. Ind. Eng. Chem. Res. 54 (48), 12187–12195. https://doi.org/10.1021/acs.iecr.5b02850.

Weniger, P., Kalkreuth, W., Busch, A., Krooss, B.M., 2010. High-pressure methane and Carbon dioxide sorption on coal and shale samples from the paraná basin, Brazil. Int. J. Coal Geol. 84 (3–4), 190–205. https://doi.org/10.1016/j.coal.2010.08.003.

Wu, K., Li, X., Guo, C., Wang, C., Chen, Z., 2016. A unified model for gas transfer in nanopores of shale-gas reservoirs: coupling pore diffusion and surface diffusion. SPE J. 21 (5), 1–29. https://doi.org/10.1021/acs.iecr.5b02850.

Zhang, Q., Wang, W.D., Kade, Y., Wang, B.T., Xiong, L., 2020. Analysis of gas transport behavior in organic and inorganic nanopores based on a unified apparent gas permeability model. Petrol. Sci. 17 (1), 168–181. https://doi.org/10.1007/s12182-019-00358-4.